Published online 14 March 2020

Nucleic Acids Research, 2020, Vol. 48, No. 8 ***4041–4051***
doi: 10.1093/nar/gkaa137

Direct observation and analysis of TET-mediated oxidation processes in a DNA origami nanochip

Xiwen Xing[1,2,*], Shinsuke Sato[2], Nai-Kei Wong[3], Kumi Hidaka[2], Hiroshi Sugiyama[2,4,*] and Masayuki Endo[2,4,*]

[1]Department of Biotechnology, Key Laboratory of Virology of Guangzhou, College of Life Science and Technology, Jinan University, Guangzhou 510632, China, [2]Department of Chemistry, Graduate School of Science, Kyoto University, Kitashirakawa-oiwakecho, Sakyo-ku, Kyoto 606-8502, Japan, [3]Department of Infectious Diseases, Shenzhen Third People's Hospital, The Second Hospital Affiliated to Southern University of Science and Technology, Shenzhen 518112, China and [4]Institute for Integrated Cell-Material Sciences, Kyoto University, Yoshida-ushinomiyacho, Sakyo-ku, Kyoto 606-8501, Japan

Received September 30, 2019; Revised February 17, 2020; Editorial Decision February 17, 2020; Accepted February 25, 2020

ABSTRACT

DNA methylation and demethylation play a key role in the epigenetic regulation of gene expression; however, a series of oxidation reactions of 5-methyl cytosine (5mC) mediated by ten-eleven translocation (TET) enzymes driving demethylation process are yet to be uncovered. To elucidate the relationship between the oxidative processes and structural factors of DNA, we analysed the behavior of TET-mediated 5mC-oxidation by incorporating structural stress onto a substrate double-stranded DNA (dsDNA) using a DNA origami nanochip. The reactions and behaviors of TET enzymes were systematically monitored by biochemical analysis and single-molecule observation using atomic force microscopy (AFM). A reformative frame-like DNA origami was established to allow the incorporation of dsDNAs as 5mC-containing substrates in parallel orientations. We tested the potential effect of dsDNAs present in the tense and relaxed states within a DNA nanochip on TET oxidation. Based on enzyme binding and the detection of oxidation reactions within the DNA nanochip, it was revealed that TET preferred a relaxed substrate regardless of the modification types of 5-oxidated-methyl cytosine. Strikingly, when a multi-5mCG sites model was deployed to further characterize substrate preferences of TET, TET preferred the fully methylated site over the hemi-methylated site. This analytical modality also permits the direct observations of dynamic movements of TET such as sliding and interstrand transfer by high-speed AFM. In addition, the thymine DNA glycosylase-mediated base excision repair process was characterized in the DNA nanochip. Thus, we have convincingly established the system's ability to physically regulate enzymatic reactions, which could prove useful for the observation and characterization of coordinated DNA demethylation processes at the nanoscale.

INTRODUCTION

5-Methylcytosine (5mC) has emerged as a major form of DNA epigenetics modifications, which modifies ∼60–80% of the CpG sites in the mammalian genome (1). 5mC plays crucial regulatory roles in aging, tumorigenesis and other disease conditions (2–8). Although DNA methylation has been well-characterized, the key enzymes driving the reversal processes are still elusive due to chemically and genetically stable structures associated with the modification. Chemically, the methyl group at the C5 position of the cytosine base has a stable carbon–carbon bond, which limits the direct elimination of the methyl group. Genetically, it is produced by *de novo* DNA methyltransferases 3A and 3B, and further held in maintenance by methyltransferase DNMT1 (8,10–12). Despite these, mammalian 5mC could still be reversed to an unmodified state in several aspects. First, untimely DNA methylation maintenance can result in the dilution of 5mC levels during DNA replication, known as passive DNA demethylation (4,13). Second, 5mC could be iteratively changed into 5-hydroxymethylcytosine (5hmC), 5-formylcytosine (5foC) and 5-carboxylcytosine (5caC), termed as ox-mC, in the presence of ten-eleven translocation (TET) proteins (Figure 1A) (8,9,14–16,18). Third, the thymine DNA glycosylase (TDG)-mediated exci-

*To whom correspondence should be addressed. Tel: +81 75 753 9765; Fax: +81 75 753 9761; Email: endo@kuchem.kyoto-u.ac.jp
Correspondence may also be addressed to Xiwen Xing. Email: xingxiwen@jnu.edu.cn
Correspondence may also be addressed to Hiroshi Sugiyama. Email: hs@kuchem.kyoto-u.ac.jp

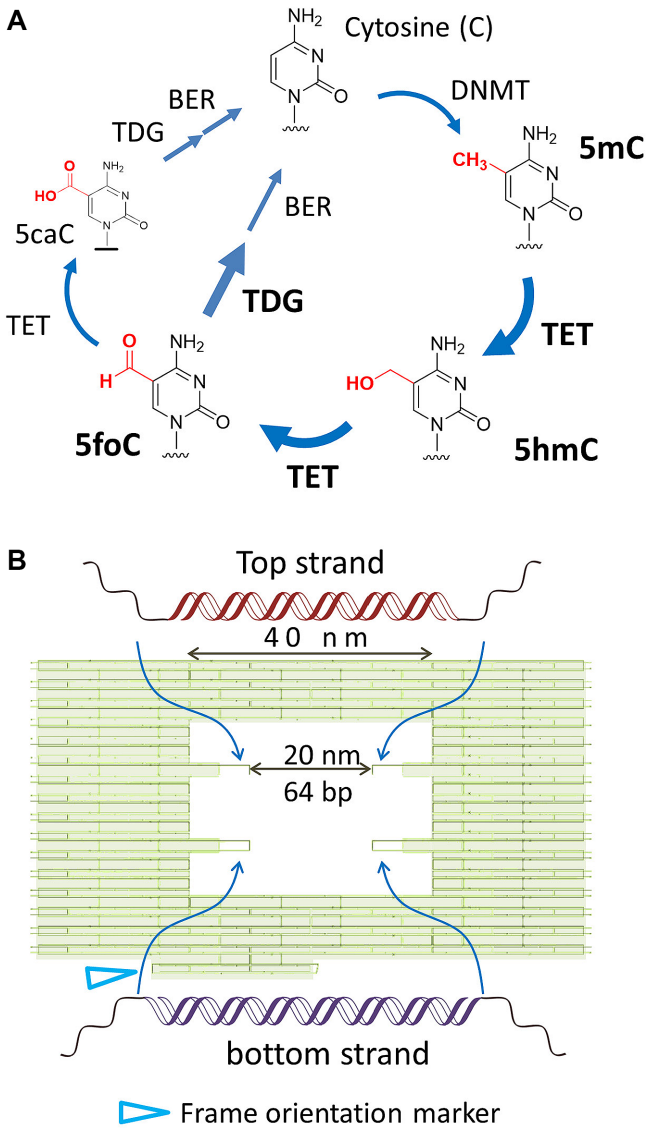

Figure 1. (**A**) An illustration of the methylation and demethylation processes involving TET and TDG. (**B**) DNA origami frame structure used in this study. Two different substrate dsDNAs were incorporated via the hybridization of single-stranded DNAs at both ends.

sion of 5foC and 5caC through a base excision repair (BER) pathway can also result in DNA demethylation, which is a well-documented active DNA demethylation mechanism (17,18). While several other active DNA demethylation mechanisms have been suggested, the TET-dependent BER mechanism has gained the most support, as the whole demethylation pathways has been demonstrated *in vitro* (19).

TET proteins are iron (II)/α-ketoglutarate [Fe (II)/α-KG)]-dependent dioxygenases (9,20,21). All three types of TET proteins, TET 1, TET 2, TET 3, share a conserved core catalytic domain at the carboxyl-terminus, which comprises a double sheet β-helix (DSBH), a cysteine-rich domain, and a CXXC domain (∼60 amino acids) in TET1 and TET3 (Supplementary Figure S1) (8,9,20,22–24). In general, with the aid of the CXXC domain, the TET enzyme can specifically recognize and target the CpG site. The DSBH domain could recruit Fe(II), α-ketoglutarate (α-KG) and ox-mC together for oxidation, while the cysteine-rich domain is likely to chelate two or more Zn^{2+} ions (via nine conserved Cys residues and 1 His residue) and stabilize the overall base-flipping structure during the TET-DNA interaction (22). Notably, a unique C-terminal catalytic domain can also oxidize 5mC and localize to the nucleus. Meanwhile, despite there are substantial studies on the functional roles of ox-mC and TET catalytic behavior, the processivity of TET actions have remained at best controversial (1,6,9,25). TET processivity can be resolved into genetic, physical and chemical aspects (Supplementary Figure S2). Genetic processivity refers to the genetic outcomes of TET-mediated actions in the genome, which is determined by various factors and gives rise to different distributions of ox-mC in individual CpG sites (26–28). Discussions about the physical processivity have focused on whether TET slides along DNA from one CpG site to another, though there was also *in vitro* evidence suggesting TET preference in a non-physical-processive manner (29). Chemical processivity refers to the ability of TET to catalyze the oxidation of 5mC iteratively to 5caC with or without releasing its substrates. For chemical processivity, one group supports a non-chemical-processive mechanism due to the symmetrically distribution of foC (30). Crawford *et al.* maintained the chemical processivity theory based on the results from an isotope-based analysis (16). At the same time, work by Tamanaha *et al.* could not totally support a non-chemical-processive mechanism as they found that DNA-bound TET did not preferentially oxidize other CpG sites on the same DNA molecule (29). One explanation for this discrepancy is that the TET function likely depends on reaction conditions (9).

In this study, we attempted to directly observe the behavior of a TET protein at a single-molecule level by an integrated atomic force microscopy (AFM)-origami approach (31–34). AFM is advantageous for the analysis of protein–DNA interactions due to its high spatial resolution and fidelity in near-physiological conditions. In conjunction with DNA origami, a DNA self-assembly technique, AFM has been proven especially useful for single-molecule studies on such subjects as chemical, photochemical, biochemical reactions and DNA conformational changes (34–39). Here, we leveraged a reformative frame-like DNA origami scaffold (DNA frame), with two 5mCG site-containing double-stranded DNAs (dsDNA) arranged in parallel orientations (Figure 1B) (31). We then varied dsDNAs in their tense and relaxed states to gauge the effects of TET oxidation on 5mC, 5hmC and 5foC and TDG excision for 5foC. Various multi-5mCG site models were used to determine the substrate preferences of TET. Finally, we monitored the dynamic movements of TET by high-speed AFM (HS-AFM) and directly observed the TET motion trails in a physical-processive manner.

MATERIALS AND METHODS

Materials

Single-stranded M13mp18 viral DNA, T4-βGT (10 units/μl), MspI (20 units/μL) and uridine-diphosphoglucose (UDP-Glc) were purchased from

New England Biolabs (Ipswich, MA, USA). TET1 was purchased from Wisegene (Chicago, IL, USA). ARP [aldehyde reactive probe; *O*-(biotinylcarbazoylmethyl) hydroxylamine] was purchased from Cayman Chemical (Ann Arbor, MI, USA). Recombinant human TDG protein was purchased from Novus Biologicals (Centennial, CO, USA). Real-time PCR mix was purchased from Takara (Kyoto, Japan). All short oligonucleotides including staple DNAs were purchased from Eurofins Genomics (Tokyo Japan). Chemically modified DNA oligonucleotides were obtained from Japan Bioservices (Saitama, Japan). Ammonium iron (II) sulfate hexahydrate, L-ascorbic acid, α-ketoglutarate, DL-dithiothreitol, adenosine triphosphate, 25% glutaraldehyde acid were purchased from Wako pure chemical industries (Kyoto, Japan). 1 M HEPES buffer (pH 7.5), 1 M Tris buffer (pH 7.6) were obtained from Sigma-Aldrich. The buffer 10× NEB 4 [500 mM potassium acetate, 200 mM Tris-acetate, 100 mM magnesium acetate, 10 mM DTT], and 10× cut smart buffer [500 mM potassium acetate, 200 mM Tris-acetate, 100 mM magnesium acetate, 1 mg/ml BSA] were provided by New England Biolabs.

DNA frame formation and integration of double-stranded DNAs

First, a DNA frame (Supplementary Figure S3) was assembled by folding 30 nM M13mp18 single-stranded DNA and 150 nM of 225 short ssDNA strands (staple DNAs listed in Supplementary Table S1) together from 85 to 15°C at a rate of −1.0°C/min in a solution (30 μl) containing 20 mM HEPES (pH 7.6), 5 mM $MgCl_2$ and 15 mM NaCl, in which TET could retain its activity. Meanwhile, the top dsDNA substrate and bottom dsDNA substrate were individually prepared to a final concentration of 1 μM in the same buffer and annealed from 85 to 15°C at a rate of −1.0°C/min. The top dsDNA substrate (5 eq) was incorporated into the DNA frame by annealing from 40 to 15°C at a rate of −1.0°C/min, and then the bottom dsDNA substrate (5 eq) was incorporated by annealing from 30 to 15°C at a rate of −1.0°C/min. After removing excess amounts of unbound dsDNAs and staples by gel filtration (900 μl Sephacryl S-300, GE Healthcare), the DNA frame with two dsDNA substrates (DNA nanochips) could be used for further experiment (Supplementary Figure S4). Attachment of the substrates in all the steps were confirmed by AFM (Supplementary Figure S5). The sequences of the incorporated dsDNAs are listed in Supplementary Table S2.

HPLC experiment for analysis of TET oxidation

A solution containing C-analogue-modified oligonucleotide (55.4 μM) and mTET1 protein (7.3 μM) were incubated at 37°C for 1 h (40). After incubation, the reaction mixture was quenched by dilution, and 3 μl of the reaction mixture was used for further HPLC analysis with a gradient program with 3–9% (v/v) acetonitrile/Milli-Q water (Supplementary Figure S6).

TET binding to substrate dsDNAs in DNA nanochip

A reaction mixture (23 μl) was prepared by mixing 15 μl DNA frame carrying two substrate dsDNAs (30 nM), 2.4 μl TET protein (3 μM), 4.35 μl 5× oxidation buffer [20 mM ATP, 40 mM DTT, 16.5 mM α-KG, 33 mM L-ascorbic acid] and 1.25 μl Fe(II) (16.3 g/mol) solution]. The ratio of DNA frame/TET was 1/15. After the sample was incubated at 37°C for 30 s, the reaction was fixed by 4 μl 1% glutaraldehyde acid (diluted with 20 mM HEPES buffer and 5 mM $MgCl_2$) at 25°C for 18 min, then the reaction was terminated by the addition of 8 μl Tris-buffer [20 mM Tris–HCl (pH 7.6) and 5 mM $MgCl_2$] at 25°C and incubated another 18 min. Then, the sample was purified by gel filtration (600 μl Sephacryl S-300, GE Healthcare) (Supplementary Figures S7 and S8). Notably, for better reactivity of TET, all the components especially Fe(II) and DTT were prepared freshly every time

AFM imaging of prefixed samples

For AFM imaging, the sample (5 μl) was deposited onto a freshly cleaved mica plate. After 10 min incubation at RT, the mica was rinsed and imaged in the same sample buffer. AFM imaging was performed by using Dimension FastScan AFM (Bruker AXS, Madison, WI, USA) with a silicon nitride cantilever with a spring constant of 0.06–0.14 N m^{-1} and resonant frequency of 98.5–140 kHz in water. Scanning was performed in the same buffer solution by using a tapping mode.

High-speed AFM imaging of TET dynamic movements

After purified the DNA frame carrying two dsDNAs, 2 μl of the mixture (diluted into 5 μM) was deposited onto a freshly cleaved mica plate for 5 min at rt, and then rinsed three times with the sample buffer solution. To the mica surface was added 2 μl of TET containing solution in which the fresh TET enzyme (stored at −80°C) was diluted into 75 nM by 5× oxidation buffer. High-speed AFM images were obtained by using a Nano Live Vision AFM (RIBM, Tsukuba, Japan) with a silicon nitride cantilever (Olympus BL-AC10EGS) with a spring constant of 0.1–0.2 N m^{-1} and resonant frequency of 400–1000 kHz in water. Scanning was performed in the 1× oxidation buffer by using a tapping mode.

TET oxidation, T4-βGT transferring and MspI cleavage of target dsDNAs in DNA nanochip

The DNA frame carrying both 64-bp and 74-bp dsDNA was purified by 900 μl gel filtration (Sephacryl S-400). The oxidation reaction was performed in a 10 μl solution containing 8 nM purified DNA frame with two substrate dsDNAs, 76 nM Fe(II), 1.5 μM TET in 1× oxidation buffer at 37°C for 60 min. Then, 2 μl of the mixture thereof was used in the subsequent T4-βGT transferring reaction (11.2 μl T4-βGT reaction system contained 0.6 μl 10× NEB 4 buffer, 10× cut smart buffer, 0.3 μl 50 × uridine-diphosphoglucose (UDP-Glc), 7 units of T4-βGT and 7 μl MilliQ water) at 37°C for 120 min. Finally, 0.8 μl MspI was added to 12 μl total volume of the above mixture, which was incubated at 37°C for another 60 min.

TET oxidation, ARP reaction and MspI cleavage of substrate dsDNAs in DNA nanochip

Preparation of DNA nanochips and TET oxidation reactions were performed by methods described above. Then, a mixture thereof (5 μl) was treated with 0.8 μl ARP (22.5 mM) and 0.5 μl anisidine (220 mM) at 25°C for 30 min (41). Finally, 0.8 μl MspI was added to 12 μl total volume of the above mixture, which was incubated for another 60 min at 37°C.

TDG reaction to substrate dsDNAs in DNA nanochip

Preparation of DNA nanochips was performed by using methods as described above. A nanochip (30 μl) was treated with TDG (1 μl, 10 μmol) at 37°C for 30 min. The mixture was treated with $NaBH_4$ (5 μl, 300 mM) at 25°C for 10 min to reduce the Schiff base linkage between TDG catalytic residue and ribose (31). Finally, covalently bound TDG was observed by AFM.

Quantification of oxidation in DNA nanochip by quantitative RT-PCR

Quantitative PCR and subsequent calculations were performed with a Takara thermal cycle dice real-time system II (Takara Bio Inc), which detects signals emitted from fluorogenic probes during PCR (35). The PCR mixture contained 12.5 μl 2× SYBR@fast qPCR mix, 800 nM forward and reverse primers, and 12 μl the mixture from the last enzyme-cascade step. Each 40-PCR cycle was programmed as a 15 s denaturation step at 95°C and 30 s elongation step at 58°C. A standard curve was obtained by using the absolute amount of 1 fmol, 100 amol, 10 amol, 1 amol, 100 zmol, 10 zmol, 1 zmol template dsDNAs. The incorporated substrate dsDNAs and primer sequences are as listed in Supplementary Table S3.

SPR experiment for characterizing TET interaction with substrate dsDNAs

SPR experiment was performed by using a BIAcore X instrument (GE Healthcare) in running buffer containing 10 mM HEPES (pH 7.4), 150 mM NaCl, 3 mM EDTA, 0.005% surfactant P20 at a flow rate of 20 μl min^{-1} at 25°C. Biotinylated-DNA as shown in Supplementary Table S4 was coupled to a SA-sensor chip (GE Healthcare) with a response of 31 units (fully-5mC) and 44 units (hemi-5mC), which was achieved by adjusting the concentration of oligonucleotides and time of contact. Mouse TET1 catalytic domain was injected into the surface of fully-5mC and hemi-5mC biotinylated DNAs in running buffer for 180 s, respectively. The surface was washed with running buffer for 60 s after dissociation of the complexes. Data were analysed by fitting all curves by using a two-state binding model as described in Supplementary Figure S15C and determining kinetics association and dissociation rate constants with BIA evaluation software. Data obtained are summarized in Supplementary Table S5.

RESULTS AND DISCUSSIONS

DNA frame formation and feasibility of reaction monitoring

The frame model used in this study consists of twist-corrected DNA origami structures (Figure 1A and Supplementary Figure S1, Supplementary Table S1). The frame possessed a vacant rectangular area (40 nm × 40 nm) in the center, in which various dsDNAs with one or multiple 5-oxidated-mC modified sites could be installed as different substrate models. Specifically, we concentrated on five operation options for analysis on the dsDNA cassette: (i) analyzing tension effects on a tension model which involved placing two different dsDNA substrates, tensed and relaxed dsDNAs, with or without an opposite nicking site; (ii) analyzing the effects of 5mC distribution on a methylation distribution model which involved introducing multi-5mCG site-containing substrates; (iii) analyzing substrate effects by installing different ox-mC substrates on the same tension-controlled model; (iv) observation of TET movements at a single-molecule level in the DNA nanochip and (v) studying the excision of a 5foC substrate by TDG in the DNA nanochip.

In order to ensure that two dsNDA substrates are arranged in a parallel orientation, we incorporated them into the experimental DNA frame by annealing, followed by AFM observation. In this way, the substrates' incorporation yield reached over 99%, which was high enough for further observation ($\eta = 217/220$, $N = 220$), and the length of the substrates was also optimized (Supplementary Figure S2A) (31,32). Typically, under the traction of divalent magnesium cation (Mg^{2+}), a negatively charged DNA frame could rest stably on the mica surface, and the two incorporated dsDNA substrate sequences retained their flexibility. This was important for monitoring the experiment, as we could distinguish the two dsDNA substrates with ease, and the flexible substrates could also react with the enzyme readily. In this study, we chose recombinant TET1 (1418–2136), due to its size, for a 40 nm scale DNA origami cavity (∼7 nm, Supplementary Figure S5B). According to previous works, TETs are large, multi-domain proteins that adopt the double-stranded β-helix (DSBH) fold characteristic of members of Fe^{2+}/α-KG-dependent dioxygenase, with a CXXC domain at its N-terminal end (42). Full-length TET1 is detected only during a short time in embryonic development, whereas adult somatic tissues weakly express the truncated TET1s (devoid of the CXXC domain) and are predicted to control epigenetic memory erasure (42,43) (Supplementary Figure S1). The presence or absence of the CXXC domain on the truncated TET1 variants only with a catalytic domain could influence catalysis of the whole reaction, while there is no CXXC domain in wild TET2 protein (6,16,29,40). In addition, in a crystal structure, the catalytic domain could only induce distortion from B-form DNA, whereas DNA is usually located above the DSBH core with an ox-mC flipped out and inserted into the catalytic cavity.

We first examined the TET reaction using the classic TET oxidation working buffer with the addition of Mg^{2+}. In the presence of typical conditions of 10 mM Mg^{2+} used for DNA origami formation, TET activity was reduced signif-

icantly (Supplementary Figures S5C, S6). Thus, we tried to find a suitable condition under which could both TET oxidation and origami formation proceed. In the beginning, we approached this by reducing the concentration of Na^+ in the classic TET oxidation system as monovalent cations could reduce frame attachment on the mica surface by competing with Mg^{2+}. A high concentration of Na^+ was found to be nonessential as the yield of 5hmC was almost invariable despite the Na^+ level being reduced (Supplementary Figure S6A). In addition, increasing Mg^{2+} concentrations could dampen the TET oxidation activity and change 5caC methylation level (Supplementary Figure S6B). The reason could be similar to the case for the inhibition of Ni(II) ion, which causes the mutations of critical Fe(II)-binding residues in TET (44). We fixed an Mg^{2+} concentration of 5 mM in the final reaction condition, as the divalent magnesium cation is necessary for origami formation.

Evaluation of substrates' tension effects on TET binding

First, we introduced uninterrupted tense 64-bp dsDNA (~20 nm) and relaxed 74-bp dsDNA (~24 nm) with the C^mCGG site in the center of the DNA cassette (Supplementary Figure 2A, sequences are listed in Supplementary Table S2). From TET crystal structure information, DNA duplex should be distorted at least 40°C for the base flipping and hydrophobic residues insertion, so that the reaction can proceed (20). The 64-bp dsDNA fitted exactly within the cavity as s tense strand, while the 74-bp strand could allow at least 60° bending and acted as a relaxed strand (31). In this setup, we fixed the TET incubation time as 30 s or it would invariably slide to a corner of the origami. The TET enzyme had relatively high reactivity, and it would dissociate to search for other substrates with an incubation time beyond 2 min (Supplementary Figure S9). We speculated that the crowded packing at the corner made it difficult for the TET enzyme to leave, and it was trapped by the crosslinking agent. Later, the amino group on TET was crosslinked with the C^mCGG site by glutaraldehyde (GA). Accordingly, TET's further movement was limited during AFM scanning, and the intermediate process could be covalently trapped in the designed nanospace (Figure 2B–D). The yields of the crosslinking for the 64- and 74-bp dsDNAs were 38.9% and 61.1% ($N = 144$), respectively (Figure 2), which were reasonable according to the crystal bending information (20,45). Remarkably, a fold-line shaped dsDNA was occasionally observed in AFM imaging during binding with a TET protein (Figure 2C). It seemed that dsDNAs were flipping out at the bending site and other areas became tighter. Then, we introduced a nicking-site five bases opposite to the C^mCGG center without a sequence change, which could reduce the tensed pressure of the tight 64-bp dsDNA. In this case, the TET binding to the 64-bp dsDNA with the nicking site increased to 44.4%, while 55.6% ($N = 338$) of TET was preferentially bound to 74-bp dsDNA. Both these results indicated that the degree of tension of dsDNAs can control TET binding in such a way that loose dsDNAs constituted a preferred substrate and that effective substrate bending was required for TET reactions.

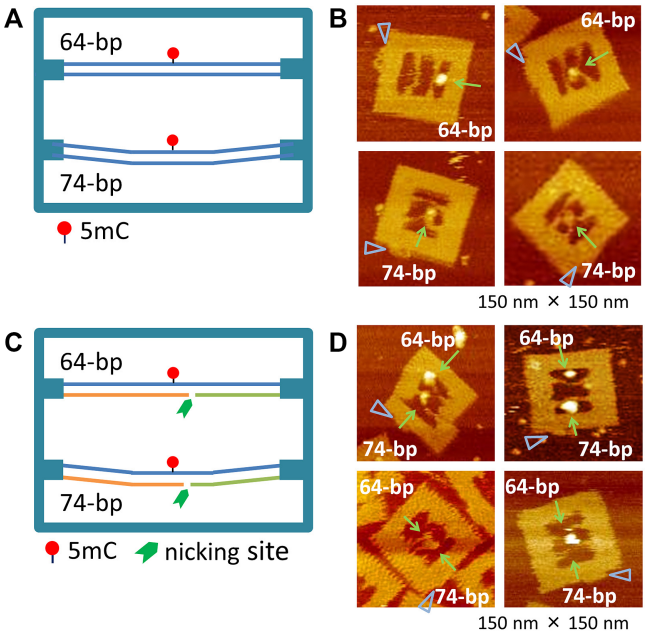

length	Substrate dsDNA	Substrate dsDNA with nicking site
64-bp (tensed)	56 (38.9%)	150 (44.4%)
74-bp (relaxed)	88 (61.1%)	188 (55.6%)

Figure 2. The tension-controlled model for TET binding analysis in a DNA nanochip. (**A**) DNA origami frame carrying different lengths (64- and 74-bp) of 5mC-modified dsDNAs. (**B**) AFM images of TET binding. (**C**) DNA origami frame carrying different lengths (64- and 74-bp) of 5mC-modified dsDNAs with a nicking site. (**D**) AFM images of TET binding. Summary of TET binding to 64- and 74-bp substrate dsDNAs. The ratio of all possible TET binding events on a DNA origami nanochip. The blue triangle in the DNA images represents the orientation marker in the DNA frame.

Biochemical analysis of the effects of substrates' tension on TET-mediated reaction

From the perspective of the reaction collision theory, only a certain percentage of molecules experience a successful collision for a chemical reaction to occur (46). We, therefore, verified the tension effects for TET oxidation by another biochemical analysis method. In general, MspI is efficient in digesting the dsDNA labelled with 5mC and 5hmC and is unable to digest 5foC and 5caC. Thus, we could readily distinguish 5mC sites from other ox-mC sites if we could protect 5hmC from MspI by transferring one glucose moiety of uridine-diphosphoglucose (UDP-Glc) to 5-hydroxymethyl group of hmC residues with T4-β-glucose transferase (T4-βGT) (Figures 3A and Supplementary Figure S10) (47). Hence, in our system, only the mC-modified dsDNA lost their sequence integrity and were not amplified by PCR, while it is possible to measure the different oxidation state for the 64- and 74-bp 5mC/5hmC-labeled sequence in the DNA origami nanochip (Figure 3A). Meanwhile, T4-βGT is a well-studied glucosyltransferase, and T4-βGT glucosylated 5hmC on ~100-nucleotide substrates efficiently and completely when the enzyme reacted in sufficient time (47).

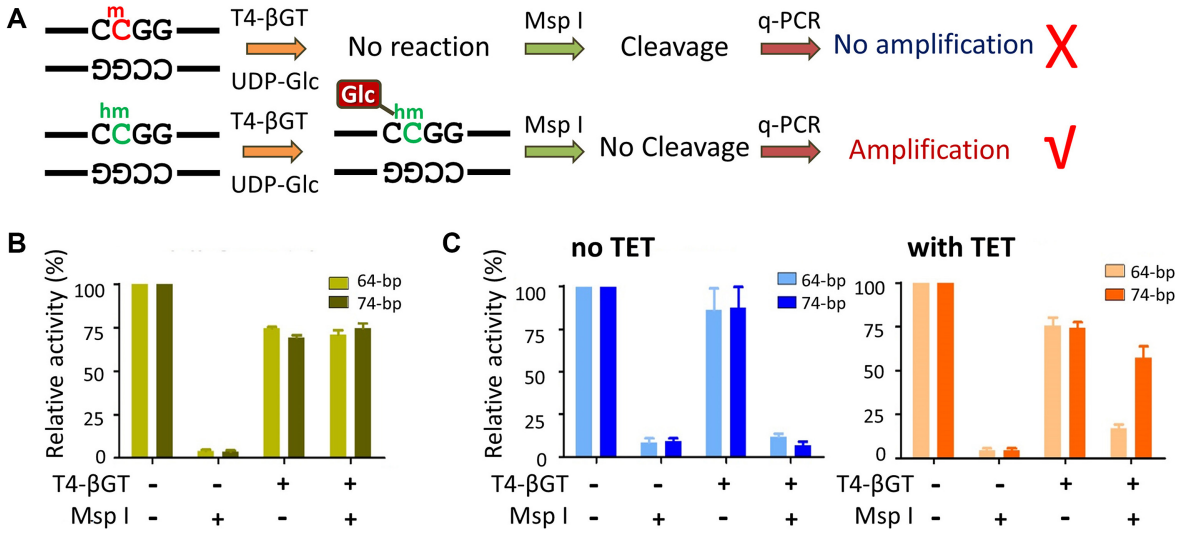

Figure 3. (**A**) A scheme showing the workflow of the biochemical analysis on TET oxidation with 5mC-dsDNA in a DNA nanochip by using T4-βGT/UTP-Glc and subsequent Msp I digestion. Outcomes of the reaction were quantified using q-PCR. (**B**) The results of q-PCR for the different lengths of 5hmC-modified substrate dsDNAs in a DNA nanochip. (**C**) The results of q-PCR for the estimation of the initial concentration of 64-bp and 74-bp 5mC-modified dsDNAs in a DNA nanochip after different sample treatments. Left: without treatment of TET; right: reaction with TET. The data shown are representative of three independent experiments.

In our detection system, a significant difference in the T4-βGT reaction was not observed between the 64-bp dsDNA substrate and 74-bp dsDNA substrate (Figure 3B). As a result, there was not much concern for the length effects in our experiments. We tested this detection system by using 5hmC-modified dsDNA substrates. The T4-βGT-treated samples prohibited the MspI cleavage, which resulted in the amplification of the strands by quantitative-polymerase chain reaction (q-PCR) (Figure 3B). We next examined the detection of TET oxidation using the 5mC-modified 64-bp and 74-bp dsDNA in the DNA nanochip (Figure 3C). Without TET treatment (Figure 3B), the samples treated with T4-βGT were digested by MspI, and the amplification level was significantly decreased. Conversely, TET reaction samples after the T4-βGT/MspI treatment showed an increase in the amplification level depending on the tension of dsDNAs (64- and 74-bp) (right graph in Figure 3C). This also shows that the 5hmC produced by TET reactions could be detected by using this system. Importantly, the intact 74-bp sequence was almost 3.3 times higher than the intact 64-bp sequence on the DNA nanochip, which meant that the oxidation efficiency for relaxed substrates was much higher. On the other hand, the data in the AFM binding situation was 1.57 times. This difference might be attributed to the difference between the binding and the subsequent reaction at the 5mC site, where the oxidation reaction needed more precise conformation around the 5mC than the binding to the substrate site. For the oxidation reaction, the tension should lower the formation of the appropriate reactive intermediate complex between TET and 5mC substrate; therefore, the oxidation reaction should be more affected and sensitive to the tension at the reaction site. Meanwhile, effective substrate bending is required for the TET-mediated 5mC→5hmC oxidation to proceed.

Thus, we aimed to quantify the effect of the tension on the substrate dsDNAs in the 5hmC→5foC step by TET oxidation. For detection of 5foC in the DNA nanochip (Supplementary Figure S11), the same strategy was adopted; the 5foC sequence could be protected from MspI by labeling a biotin group with ARP [aldehyde reactive probe; *O*-(biotinylcarbazoylmethyl) hydroxylamine] (Figure 4A and Supplementary Figure S12) (48). The 5hmC and 5foC containing substrates could be distinguished by the treatment with ARP and subsequent MspI digestion (Supplementary Figure S13), and q-PCR amplification worked for the detection of 5foC-modified dsDNAs (Figure 4B). We examined the detection of 5hmC-modified 64- and 74-bp dsDNA in the DNA nanochip (Figure 4C). Without TET treatment (Figure 4B), the amplification level of the substrates treated with ARP/MspI significantly decreased. Alternatively, the substrates after TET reaction and ARP/MspI treatment showed an increase in the amplification level depending on the tension of dsDNAs, similar to the case for the 5mC→5hmC step (right graph in Figure 4C). This time, the activity of the intact 74-bp sequence was almost 2.6 times higher than that of the 64-bp sequence, which indicated that the activity of the relaxed substrates in the 5hmC→5foC step was also better than that of the tense substrates (Figure 4B). Collectively, these results showed that the tension of dsDNA imposed in the DNA nanochip could control the oxidation activity of a TET enzyme, and bending of the dsDNAs was an important physical factor for TET reactions.

Analysis of methylation distribution effects on TET behaviors

We also compared TET binding to different ox-mC modification sequences using AFM (Schemes are shown in Figure 5A). Statistical results suggested that there were no significant differences between different ox-mC substrates in the TET binding step (Supplementary Figure S14), which was consistent with the surface plasmon resonance (SPR)

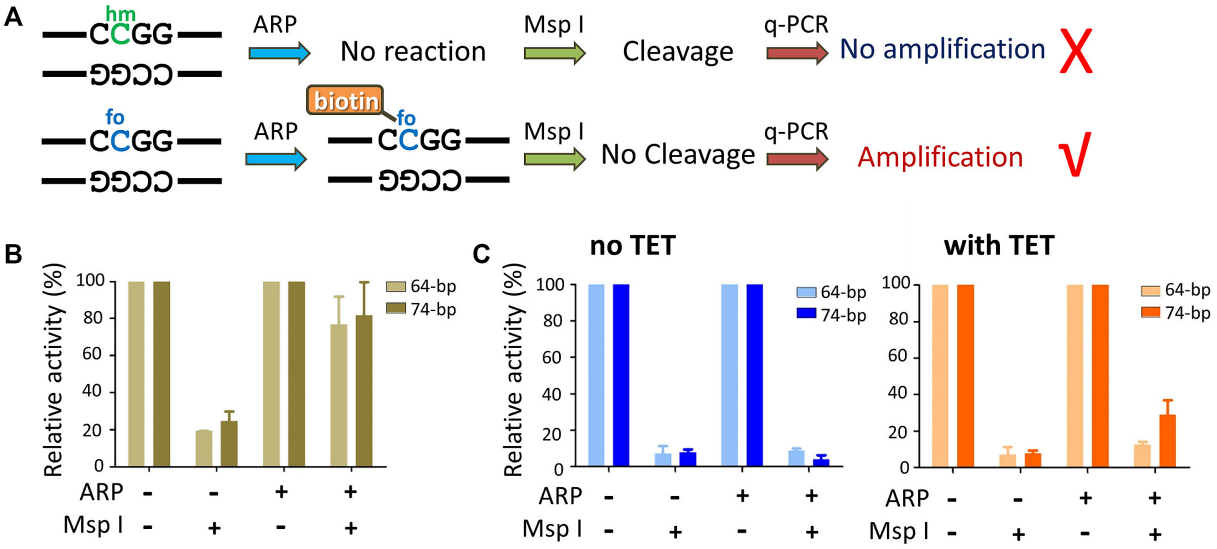

Figure 4. (**A**) A scheme showing the workflow of the biochemical analysis on TET oxidation with 5hmC-dsDNA in a DNA nanochip by using ARP (aldehyde reactive probe) labeling and subsequent Msp I digestion. Outcomes of the reaction were quantified by using q-PCR. (**B**) The results of q-PCR for the 5foC-modified substrate dsDNAs. (**C**) The results of q-PCR for estimation of the initial concentration of 64-bp and 74-bp hmC-modified dsDNAs in a DNA nanochip after different sample treatments. Left: without treatment of TET; right: reaction with TET. The data shown are representative of three independent experiments.

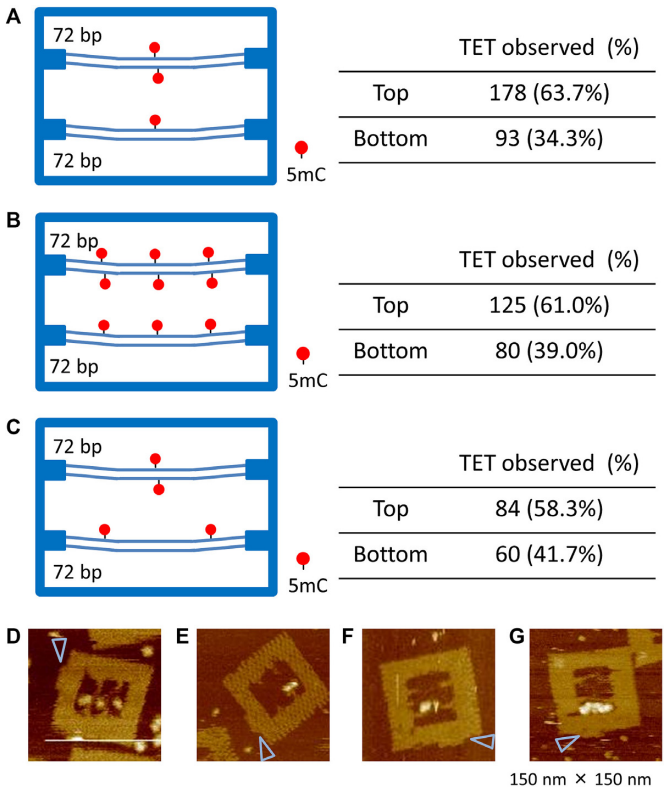

Figure 5. TET preferences for binding to fully methylated 5mC and hemi-methylated 5mC substrates. Illustration of multi-methylated 72-bp dsDNAs incorporated in the top and bottom positions of the nanochip. (**A**) One fully methylated 5mC site and one hemi- methylated 5mC site. (**B**) Three fully methylated 5mC sites and three hemi-methylated 5mC sites. (**C**) One fully methylated 5mC site and two hemi-methylated 5mC sites. The results of the counts are shown on the right side. (**D**–**G**) AFM images for TET binding in the multi-methylated model. Blue triangle: orientation marker of the bottom frame.

results in previous reports (45). These results corroborated the validity of our method for calculating the binding rate. Then, we examined the different binding behaviors between the fully-methylated site and hemi-methylated site by incorporating two 72-bp mC-modified dsDNA sets (Figure 5A). Though there are two methylation sites in a fully-methylated sequence, the chance to encounter a TET was almost the same compared to that in case of a hemi-methylated sequence in the expansive buffer within 30 s. Our results further suggested that a fully-methylated sequence has an obvious advantage in binding to the TET enzyme (65.3%, $N = 271$), and the ratio is even higher than that in the case of the situation for the TET binding to the 74-bp versus 64-bp sequence. Then, we conducted the same experiment by using a triple-methylated site model, which turned out that still more TET enzymes were bound to fully methylated sequences (61.0%, $N = 205$). In the case of a multiple methylated-site situation, it was probabilistically more favorable for TET proteins to meet substrates in a one-frame space, such that the gap could be shortened (Figure 5B). To clarify the impact of different methylation amounts between the fully methylated and hemi-methylated substrates, we compared one fully-methylated site with two separate hemi-methylated substrates in one nanochip (Figure 5C). Interestingly, the TET-binding tendency was still the same, and 58.3% of the TET proteins were bound to the fully-methylated site ($N = 144$). This observation implied that the TET enzyme indeed prefers fully-methylated sites. It also seemed reasonable to infer that differences exist in TET recognition between fully-methylated sequences and hemi-methylated sequences.

We next examined the association and dissociation of TET to hemi/fully methylated DNA substrates using SPR (Supplementary Figure S15 and Supplementary Table S5).

In this experiment, we used a two-state reaction model in which one TET protein formed a TET-DNA complex followed by changing its conformation. For simplicity, it is assumed that complex AB* could not dissociate directly into A+B without the state AB (A is TET, B is mC-dsDNA, B* is ox-mC-dsDNA). The results suggested that the association rate constant for the formation of the AB state (k_{a1}) is almost the same for both fully-5mC and hemi-5mC sequences. However, for the dissociation step, the fully-5mC sequence is almost four times smaller than the hemi-5mC sequence (k_{d2}), which meant that the affinity for TET to the fully-methylated site was better than that to the hemi-methylated site. This could explain why we observed more cases of TET binding on the fully-methylated site in the AFM observation.

Interestingly, during the AFM observation, we occasionally found a fully-methylated site simultaneously bound to two TET proteins (Figures 5D and E). Consecutive TET proteins also bound at triple-methylated sequences (Figures 5F and G), and sometimes, two close TET proteins were bound with different two sequences (Figure 5E). This might indicate that TET binding was almost undisturbed by other TET proteins, which raised the possibility of observing both the dynamic change and TET competition.

Direct observation of TET movements in DNA nanochip via high-speed AFM

We next used a high-speed AFM (HS-AFM) system to further analyze the dynamic movement of TET protein directly without crosslinking and acquired successive images. We have previously reported that the direct observation of the movements and reactions of the DNA binding proteins and DNA modifying enzymes with substrate dsDNAs in the DNA origami nanochips. Here, we used the single site fully- and hemi-methylated model shown in Figure 4A to examine the TET movement. We observed the diffusive movement of TET on the dsDNAs, which corresponded to a series of TET motions on the nanochip, such as attachment to dsDNA, sliding on dsDNA, stalling on a substrate, and dissociation from dsDNA (Figure 6A and Supplementary Figure S16A). TET enzyme stalled transiently at the center, where 5mC was incorporated, and dissociated from the dsDNA. Although the sliding movement of TET on the dsDNAs was modest because of the limited length of the substrate dsDNAs and interaction with the mica surface, the expected movements can be monitored in the DNA nanochip. In addition, movements of TET between two strands were monitored (Figure 6B). In this case, TET moved from a bottom substrate to a top substrate (image 3) and started to slide on dsDNA. Then, the TET enzyme moved to the bottom substrate (images 19–22) and finally slid on the bottom dsDNA. Such inter-strand transfer (jumping) was also observed in the other DNA binding proteins and enzymes (31,49,50). We employed relatively relaxed dsDNAs, and two strands of such dsDNAs were close to the center of the DNA frame, which allowed the visualization of TET transferred to the other strand. We previously reported the observation of the Cre-mediated DNA recombination by using 72-bp dsDNA substrates and a Holiday junction in a DNA nanochip (37), therefore, the two 72-bp dsDNAs approached in the center to facilitate the transfer of TET from one dsDNA to another.

Through monitoring successive images, a single TET enzyme was visualized to move both dsDNAs in the same nanochip, which may efficiently find the target oxidized CpG site repeatedly. This finding supported physical processivity, which refers to the capacity of the TET enzyme to slide along DNA from one CpG site to another. Meanwhile, in both Figure 6B and Supplementary Figure S16B, some TET was first bound at one of the fully-methylated sites. Then, it changed its position to the opposite 5mC at the same fully-methylated site. The entire moving processes indicated that the nanochip was an ideal model for observation and characterization of the behavior of TET enzymes. These precise single-molecule images provided us more information about TET enzymes.

TDG binding analysis on the substrate's tension-controlled model

We next investigated the reaction in the further oxidation states including 5foC and 5caC, which can be a substrate for thymine DNA glycosylase (TDG) in the initial base excitation repair (BER) pathway. We used the 5foC-containing substrate and analyzed the effect of the tension on the TDG reaction in the DNA nanochip. Before examining the TDG binding on the DNA origami model, we first used the traditional hot-alkali method to evaluate the activity of TDG (Supplementary Figure S17). When an abasic (AP) site appeared at the 5foC site, the substrate dsDNA could be cleaved by the hot alkali treatment. We observed that the 5foC-containing strand was efficiently cleaved using this procedure (Supplementary Figure S17).

We then introduced uninterrupted tensed 64-bp dsDNA and relaxed 74-bp dsDNA with $C^{fo}CGG$ at the center onto the DNA cassette for observation of the TDG reaction (Figure 7A). During the reaction, the catalytic residue of TDG should covalently bind to the ribose after the removal of the mutated base, and then $NaBH_4$ is added to reduce the unstable Schiff base linkage (31). We employed this method to characterize the reactivity for the 5foC-substrates. After the treatment, we observed that the TDG covalently bound to the substrate dsDNAs (Figure 7B). The percentage of TDG binding for the 64- and 74-bp dsDNAs was 44.3% and 55.7% ($N = 144$), respectively. The results also showed that the relaxed 74-bp dsDNA was a better substrate for TDG than that in the tensed 64-bp dsDNA. In the initial step of the BER, the reactivity can also be controlled and monitored in the DNA nanochip.

CONCLUSION

A major gap remains in our current understanding of the dynamic nature of TET movements at the enzyme-DNA interface. Advanced analytical strategies are needed to illuminate TET-mediated oxidation processes at a single-molecule resolution. In this study, we have convincingly analyzed the behavior of TET-mediated oxidation of 5-methylcytosine by using a tension-controlled and methylation distribution-controlled model and established the importance of bend-

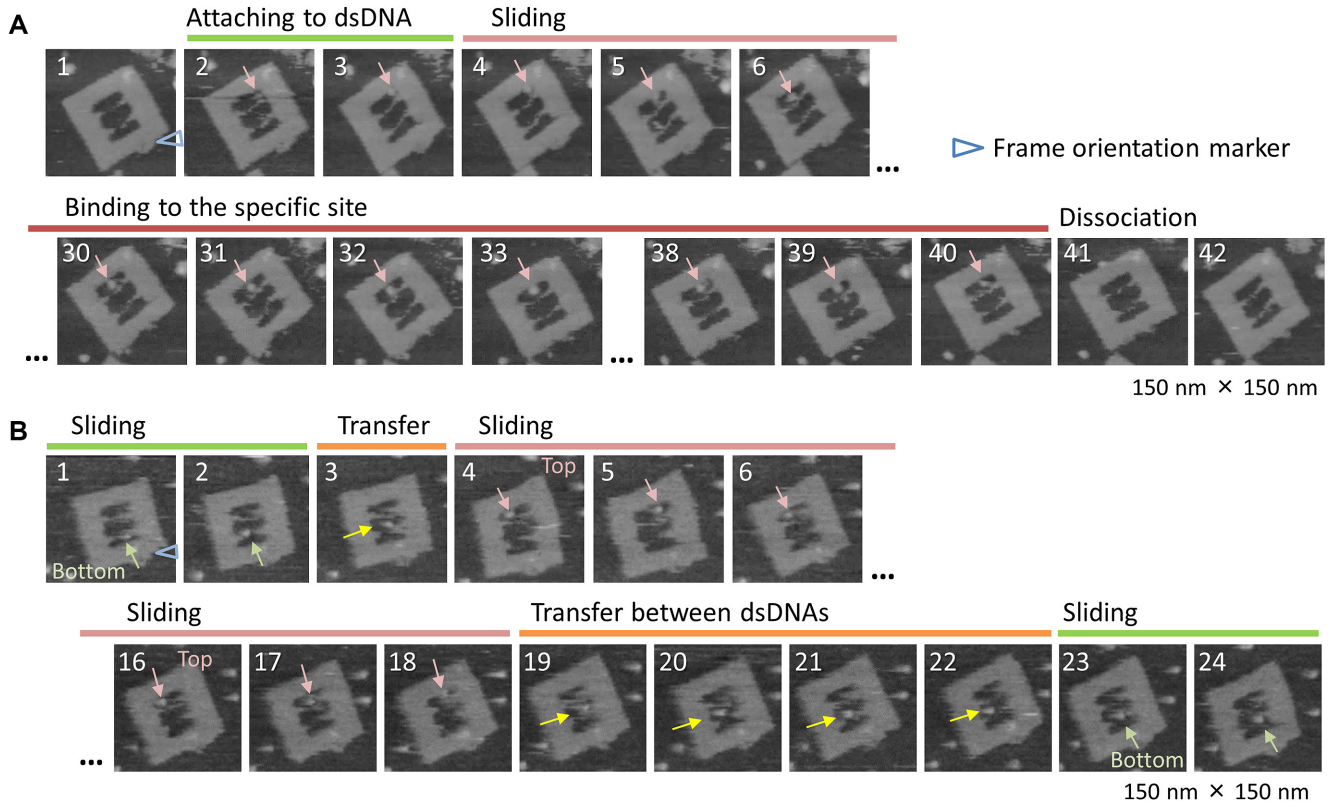

Figure 6. Successive HS-AFM images for observation of TET behaviors in a DNA frame. (**A**) TET attachment to dsDNA, sliding on dsDNA, binding to a specific site, and its dissociation. (**B**) TET sliding and transfer between two dsDNAs. Scanning 0.2 frame/s. Blue triangle: orientation marker of frame.

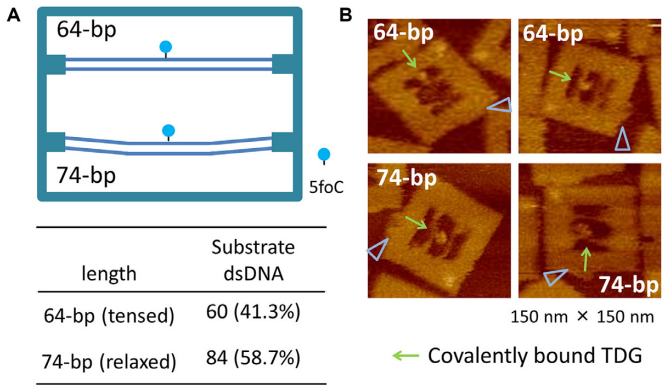

length	Substrate dsDNA
64-bp (tensed)	60 (41.3%)
74-bp (relaxed)	84 (58.7%)

Figure 7. Tension-controlled model for TDG reaction analysis in the DNA nanochip. (**A**) The DNA origami frame carrying different lengths (64- and 74-bp) of 5foC-containing dsDNAs. (**B**) AFM images of covalently bound TDG. The blue triangle in the DNA images represents the DNA frame orientation marker.

ing for a duplex during TET oxidation processes. For observation of the behavior and reaction of the TET enzyme in a DNA origami nanochip, we optimized the reaction conditions to preserve oxidation reactivity. The TET protein evidently preferred a fully-methylated site over a hemi-methylated site according to both AFM and SPR results. In addition, we also appraised a series of catalytic reactions of TET by using tense and relaxed dsDNAs as substrates constructed in a DNA nanochip. We also observed a series of dynamic motions of TET enzymes, such as the association to dsDNA, searching on the substrate dsDNA, binding to the target site, interstrand transfer (jumping), and dissociation from the dsDNA. For the catalysis of TET, stepwise oxidation reactions required repeated TET binding to the substrate CpG site. From single static AFM images, it is relatively challenging to distinguish oxidation processes. Meanwhile, an enzymatic cascade such as TET1 and TDG interaction to connect 5mC-oxidation and initial BER might be also visualized in the same approach (19). Thus, our DNA nanochip system described herein could analyze DNA demethylation processes and visualize related physical processivity at the same time. DNA origami assemblies coupled to high-speed molecular imaging provide unique opportunities for visualizing protein-DNA dynamics at an unprecedented resolution. Overall, our work has advanced a robust strategy for physically regulating TET enzyme reactions which may be applicable to further characterization of physical and biochemical attributes of protein–DNA interactions at the nanoscale.

SUPPLEMENTARY DATA

Supplementary Data are available at NAR Online.

FUNDING

JSPS KAKENHI Fund for the Promotion of Joint International Research (Fostering Joint International Research

(B) [18KK0139, 16H06356]; Uehara Memorial Foundation; Nakatani Foundation; Heiwa Nakajima Foundation (to M.E.); National Natural Science Foundation of China [21708014, 21977122]. Funding for open access charge: Uehara Memorial Foundation.
Conflict of interest statement. None declared.

REFERENCES

1. Spruijt,C.G., Gnerlich,F., Smits,A.H., Pfaffeneder,T., Jansen,P.W., Bauer,C., Munzel,M., Wagner,M., Muller,M. and Khan,F. (2013) Dynamic readers for 5-(hydroxy)methylcytosine and its oxidized derivatives. *Cell*, **152**, 1146–1159.
2. Schübeler,D. (2015) Function and information content of DNA methylation. *Nature*, **517**, 321–326.
3. Bird,A. (2002) DNA methylation patterns and epigenetic memory. *Genes Dev.*, **16**, 6–21.
4. Dalton,S.R. and Bellacosa,A. (2012) DNA demethylation by TDG. *Epigenomics*, **4**, 459–467.
5. Jones,P.A. (2012) Functions of DNA methylation: islands, start sites, gene bodies and beyond. *Nat. Rev. Genet.*, **13**, 484–492.
6. Tahiliani,M., Koh,K.P., Shen,Y., Pastor,W.A., Bandukwala,H., Brudno,Y., Agarwal,S., Iyer,L.M., Liu,D.R., Aravind,L. *et al.* (2009) Conversion of 5-methylcytosine to 5-hydroxymethylcytosine in mammalian DNA by MLL partner TET1. *Science*, **324**, 930–935.
7. Huang,Y., Chavez,L., Chang,X., Wang,X., Pastor,W.A., Kang,J., Zepeda-Martínez,J.A., Pape,U.J., Jacobsen,S.E., Peters,B. *et al.* (2014) Distinct roles of the methylcytosine oxidases Tet1 and Tet2 in mouse embryonic stem cells. *Proc. Natl. Acad. Sci. U.S.A.*, **111**, 1361–1366.
8. Kohli,R.M. and Zhang,Y. (2013) TET enzymes, TDG and the dynamics of DNA demethylation. *Nature*, **502**, 472–479.
9. Wu,X. and Zhang,Y. (2017) TET-mediated active DNA demethylation: mechanism, function and beyond. *Nat. Rev. Genet.*, **18**, 517–534.
10. Hermann,A., Goyal,R. and Jeltsch,A. (2004) The Dnmt1 DNA-(cytosine-C5)-methyltransferase methylates DNA processively with high preference for hemimethylated target sites. *J. Biol. Chem.*, **279**, 48350–48359.
11. Bostick,M., Kim,J.K., Estève,P.O., Clark,A., Pradhan,S. and Jacobsen,S.E. (2007) UHRF1 plays a role in maintaining DNA methylation in mammalian cells. *Science*, **317**, 1760–1764.
12. Xing,X.W., Tang,F., Wu,J., Chu,J.M., Feng,Y.Q., Zhou,X. and Yuan,B.F. (2014) Sensitive detection of DNA methyltransferase activity based on exonuclease-mediated target recycling. *Anal. Chem.*, **86**, 11269–11274.
13. Inoue,A., Shen,L., Dai,Q., He,C. and Zhang,Y. (2011) Generation and replication-dependent dilution of 5fC and 5caC during mouse preimplantation development. *Cell Res.*, **21**, 1670–1676.
14. Jones,P.A. (2012) Functions of DNA methylation: islands, start sites, gene bodies and beyond. *Nat Rev. Genet.*, **13**, 484–492.
15. Ito,S., Shen,L., Dai,Q., Wu,S.C., Collins,L.B., Swenberg,J.A., He,C. and Zhang,Y. (2011) Tet proteins can convert 5-methylcytosine to 5-formylcytosine and 5-carboxylcytosine. *Science*, **333**, 1300–1303.
16. Crawford,D.J., Liu,M.Y., Nabel,C.S., Cao,X.J., Garcia,B.A. and Kohli,R.M. (2016) Tet2 catalyzes stepwise 5-methylcytosine oxidation by an iterative and de novo mechanism. *J. Am. Chem. Soc.*, **138**, 730–733.
17. Maiti,A. and Drohat,A.C. (2011) Thymine DNA glycosylase can rapidly excise 5-formylcytosine and 5-carboxylcytosine: potential implications for active demethylation of CpG sites. *J. Biol. Chem.*, **286**, 35334–35338.
18. He,Y.F., Li,B.Z., Li,Z., Liu,P., Wang,Y., Tang,Q., Ding,J., Jia,Y., Chen,Z. and Li,L. (2011) Tet-mediated formation of 5-carboxylcytosine and its excision by TDG in mammalian DNA. *Science*, **333**, 1303–1307.
19. Weber,A.R., Krawczyk,C., Robertson,A.B., Kusnierczyk,A., Vagbo,C.B., Schuermann,D., Klungland,A. and Schar,P. (2016) Biochemical reconstitution of TET1-TDG-BER-dependent active DNA demethylation reveals a highly coordinated mechanism. *Nat. Commun.*, **7**, 10806.
20. Hu,L., Li,Z., Cheng,J., Rao,Q., Gong,W., Liu,M., Shi,Y.G., Zhu,J., Wang,P. and Xu,Y. (2013) Crystal structure of TET2-DNA complex: insight into TET-mediated 5mC oxidation. *Cell*, **155**, 1545–1555.
21. Mahfoudhi,E., Talhaoui,I., Cabagnols,X., Della,Valle, V., Secardin,L., Rameau,P., Bernard,O.A., Ishchenko,A.A., Abbes,S. and Vainchenker,W. (2016) TET2-mediated 5-hydroxymethylcytosine induces genetic instability and mutagenesis. *DNA Repair (Amst.)*, **43**, 78–88.
22. Pastor,W.A., Aravind,L. and Rao,A. (2013) TETonic shift: biological roles of TET proteins in DNA demethylation and transcription. *Nat. Rev. Mol. Cell Biol.*, **14**, 341–356.
23. D'Annessa,I., Coletta,A., Sutthibutpong,T., Mitchell,J., Chillemi,G., Harris,S. and Desideri,A. (2014) Simulations of DNA topoisomerase 1B bound to supercoiled DNA reveal changes in the flexibility pattern of the enzyme and a secondary protein–DNA binding site. *Nucleic Acids Res.*, **42**, 9304–9312.
24. Vella,P., Scelfo,A., Jammula,S., Chiacchiera,F., Williams,K., Cuomo,A., Roberto,A., Christensen,J., Bonaldi,T. and Helin,K.. (2013) Tet proteins connect the O-linked N-acetylglucosamine transferase Ogt to chromatin in embryonic stem cells. *Mol. Cell*, **49**, 645–656.
25. Wang,L., Zhou,Y., Xu,L., Xiao,R., Lu,X., Chen,L., Chong,J., Li,H., He,C. and Fu,X.D. (2015) Molecular basis for 5-carboxycytosine recognition by RNA polymerase II elongation complex. *Nature*, **523**, 621–625.
26. Shen,L., Wu,H., Diep,D., Yamaguchi,S., D'Alessio,A.C., Fung,H.L., Zhang,K. and Zhang,Y. (2013) Genome-wide analysis reveals TET- and TDG-dependent 5-methylcytosine oxidation dynamics. *Cell*, **153**, 692–706.
27. Sun,Z., Dai,N., Borgaro,J.G., Quimby,A., Sun,D., Correa,I.R. Jr, Zheng,Y., Zhu,Z. and Guan,S. (2015) A sensitive approach to map genome-wide 5-hydroxymethylcytosine and 5-formylcytosine at single-base resolution. *Mol. Cell*, **57**, 750–761.
28. Xia,B., Han,D., Lu,X., Sun,Z., Zhou,A., Yin,Q., Zeng,H., Liu,M., Jiang,X. and Xie,W. (2015) Bisulfite-free, base-resolution analysis of 5-formylcytosine at the genome scale. *Nat. Methods*, **12**, 1047–1050.
29. Tamanaha,E., Guan,S., Marks,K. and Saleh,L. (2016) Distributive Processing by the Iron(II)/α-Ketoglutarate-Dependent Catalytic Domains of the TET Enzymes Is Consistent with Epigenetic Roles for Oxidized 5-Methylcytosine Bases. *J. Am. Chem. Soc.*, **138**, 9345–9348.
30. Xu,L., Chen,Y.C., Chong,J., Fin,A., McCoy,L.S., Xu,J., Zhang,C. and Wang,D. (2014) Pyrene-based quantitative detection of the 5-formylcytosine loci symmetry in the CpG duplex content during TET-dependent demethylation. *Angew. Chem. Int. Ed.*, **53**, 11223–11227.
31. Endo,M., Katsuda,Y., Hidaka,K. and Sugiyama,H. (2010) A versatile DNA nanochip for direct analysis of DNA base-excision repair. *Angew. Chem. Int. Ed.*, **49**, 9412–9416.
32. Endo,M., Katsuda,Y., Hidaka,K. and Sugiyama,H. (2010) Regulation of DNA methylation using different tensions of double strands constructed in a defined DNA nanostructure. *J. Am. Chem. Soc.*, **132**, 1592–1597.
33. Endo,M. and Sugiyama,H. (2014) Single-molecule imaging of dynamic motions of biomolecules in DNA origami nanostructures using high-speed atomic force microscopy. *Acc. Chem. Res.*, **47**, 1645–1653.
34. Rajendran,A., Endo,M., Hidaka,K., Tran,P.L., Mergny,J.L., Gorelick,R.J. and Sugiyama,H. (2013) HIV-1 nucleocapsid proteins as molecular chaperones for tetramolecular antiparallel G-quadruplex formation. *J. Am. Chem. Soc.*, **135**, 18575–18585.
35. Raz,M.H., Hidaka,K., Sturla,S.J., Sugiyama,H. and Endo,M. (2016) Torsional constraints of DNA substrates impact cas9 cleavage. *J. Am. Chem. Soc.*, **138**, 13842–13845.
36. Rajendran,A., Endo,M. and Sugiyama,H. (2014) State-of-the-art high-speed atomic force microscopy for investigation of single-molecular dynamics of proteins. *Chem Rev.*, **114**, 1493–1520.
37. Suzuki,Y., Endo,M., Katsuda,Y., Ou,K., Hidaka,K. and Sugiyama,H. (2014) DNA origami based visualization system for studying site-specific recombination events. *J. Am. Chem. Soc.*, **136**, 211–218.
38. Yamamoto,S., De,D., Hidaka,K., Kim,K.K., Endo,M. and Sugiyama,H. (2014) Single molecule visualization and characterization of Sox2-Pax6 complex formation on a regulatory

DNA element using a DNA origami frame. *Nano Lett.*, **14**, 2286–2292.
39. Endo,M., Xing,X., Zhou,X., Emura,T., Hidaka,K., Tuesuwan,B. and Sugiyama,H. (2015) Single-molecule manipulation of the duplex formation and dissociation at the G-quadruplex_i-motif site in the DNA nanostructure. *ACS Nano*, **9**, 9922–9929.
40. Kizaki,S. and Sugiyama,H. (2014) CGmCGCG is a versatile substrate with which to evaluate Tet protein activity. *Org. Biomol. Chem.*, **12**, 104–107.
41. Wang,S.R., Wang,J.Q., Fu,B.S., Chen,K., Xiong,W., Wei,L., Qing,G., Tian,T. and Zhou,X. (2018) Supramolecular Coordination-Directed Reversible Regulation of Protein Activities at Epigenetic DNA Marks. *J. Am. Chem. Soc.*, **140**, 15842–15849.
42. Parker,M.J., Weigele,P.R. and Saleh,L. (2018) Insights into the biochemistry, evolution, and biotechnological applications of the Ten-Eleven translocation (TET) Enzymes. *Biochemistry*, **58**, 450–467.
43. Zhang,W., Xia,W., Wang,Q., Towers,A.J., Chen,J., Gao,R., Zhang,Y., Yen,C.A., Lee,A.Y. and Li,Y.(2016) Isoform switch of TET1 regulates DNA demethylation and mouse development. *Mol. Cell*, **64**, 1062–1073.
44. Yin,R., Mo,J., Dai,J. and Wang,H. (2017) Nickel(II) inhibits tet-mediated 5-methylcytosine oxidation by high affinity displacement of the cofactor iron(II). *ACS Chem. Biol.*, **12**, 1494–1498.
45. Hu,L., Lu,J., Cheng,J., Rao,Q., Li,Z., Hou,H., Lou,Z., Zhang,L., Li,W. and Gong,W.(2015) Structural insight into substrate preference for TET-mediated oxidation. *Nature*, **527**, 118–122.
46. Jia,H., Zhu,G. and Wang,P. (2003) Catalytic behaviors of enzymes attached to nanoparticles: the effect of particle mobility. *Biotechnol. Bioeng.*, **84**, 406–414.
47. Song,C.X., Szulwach,K.E., Fu,Y., Dai,Q., Yi,C., Li,X., Li,Y., Chen,C.H., Zhang,W. and Jian,X.(2011) Selective chemical labeling reveals the genome-wide distribution of 5-hydroxymethylcytosine. *Nat. Biotechnol.*, **29**, 68–72.
48. Raiber,E.A., Beraldi,D., Ficz,G., Burgess,H.E., Branco,M.R., Murat,P., Oxley,D., Booth,M.J., Reik,W. and Balasubramanian,S. (2012) Genome-wide distribution of 5-formylcytosine in embryonic stem cells is associated with transcription and depends on thymine DNA glycosylase. *Genome Biol.*, **13**, R69.
49. Lee,A.J., Endo,M., Hobbs,J.K. and Walti,C. (2018) Direct single-molecule observation of mode and geometry of RecA-mediated homology search. *ACS Nano*, **12**, 272–278.
50. Raghavan,G., Hidaka,K., Sugiyama,H. and Endo,M. (2019) Direct observation and analysis of the dynamics of the photoresponsive transcription factor GAL4. *Angew. Chem. Int. Ed.*, **58**, 7626–7630.